Modelling and Performance Analysis of Photoconductive Antennas for THz Generation

Master Thesis
submitted to the Faculty of the
Escola Tècnica d'Enginyeria de Telecomunicació de Barcelona
Universitat Politècnica de Catalunya
by

David Schönenberger

In partial fulfillment
of the requirements for the master in
ENGINEERING PHYSICS

Advisor:
Dr. Santos Blanco, Maria Concepción,
Lopez Menchon, Hector
Barcelona, Date 02/07/2022

telecos
BCN

Contents

List of Figures

Listings

List of Tables

Abstract

Photoconductive antennas are devices capable of generating THz waves. In this thesis, we propose a model of THz wave generation in photoconductive antennas based on the Dude model. The derived equations explain the THz radiation when a optical pulse illuminates a photoconductor with an applied bias field. Furthermore, we derive an additional term appearing in the Drude equation that accounts for the generation of carriers with zero velocity. The model includes space-charge screening through a geometrical factor and radiation screening through an effective antenna impedance. The system is solved numerically using the iterative fixed-point method and Anderson acceleration. The fixed-point method convergence is limited, but Anderson acceleration can converge for a broader range of parameters. Analyzing the photocurrent at different optical powers, we find that it saturates at high optical powers due to the slowdown of the dynamics by the screening fields.

1 Introduction

Since the discovery of electromagnetic waves (EM waves), several studies have led to their controlled emission, their detection, and exploitation for a variety of purposes. Today, they are used for communication (radio, wireless internet, mobile phones,...) and imaging and study of materials based on their interactions with the EM waves. The properties and applications of EM waves are very much dependent on their frequency. Therefore, we can classify them into several groups (Radio waves, infrared, visible, ultraviolet, X rays, and Gamma rays, Fig. 1). Among them, a particular band stands out due to the lack of natural terrestrial sources, the Terahertz band. Terahertz electromagnetic radiation or submillimetre radiation lies between the high-frequency microwave band (300 gigahertz) and the long-wavelength edge of infrared light (3000 gigahertz), i.e., between the wavelengths of 0.1 mm infrared to 1.00 mm. Despite having several uses, this band is the less studied range of EM waves [7]. In particular, astronomers and space scientists have used it for about twenty years because "98% of the photons emitted since the Big Bang are in the submillimetre band" (P. Siegel, [20]). In the medical field, Terahertz wave radiation can penetrate many organic materials without causing the same damage as X-rays and other ionizing radiation. Moreover, dielectrics and intrinsic semiconductors are transparent in the THz band, while metals have very high reflectivity in the 1 THz frequency. Polar substances, such as water, have a high absorption rate ($\alpha \approx 250\,\mu\mathrm{m}^{-1}$ at 1 THz for liquid water). These properties arouse interest in the Terahertz band for its potential uses in quality control and biomedical imaging or scanning bombs and explosives at airports [7].
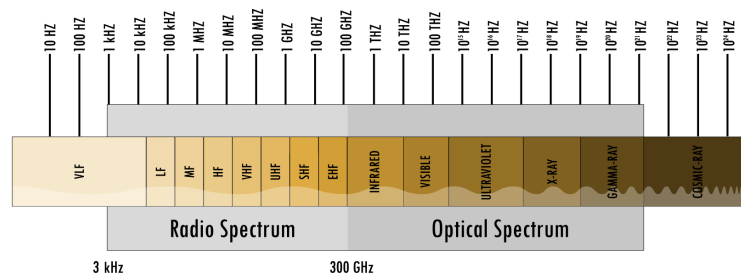
Figure 1: EM spectrum

There are various efficient ways to generate and detect EM waves in both the ranges of microwaves and the optical domain. Advances in optics and electronics have led to different sources of THz frequencies, such as P-Type Ge lasers and quantum cascades lasers [2] that generate high-power THz radiation. In addition, relativistic electrons generate extremely bright broadband THz radiation because of their quick acceleration [1]. However, these sources tend to be very expensive and usually extensive in size [6]. As an alternative, photoconductive antennas (PCA) offer a cheaper and lighter source of THz radiation thanks to their fast varying processes [3]. Unfortunately, current PCA technology is low in efficiency.

The main objective is to create a physical model for a THz-band PCA transmitter to

improve and optimize its performance and efficiency. In this thesis, we derive a model for PCA based on the Drude model. As a novelty, we solve the nonlinear set of equations numerically using a robust and reliable accelerated fixed-point method. Finally, we discuss the validity of the model and results obtained, commenting on the potential improvements.

1.1 Design of PCA for THz generation
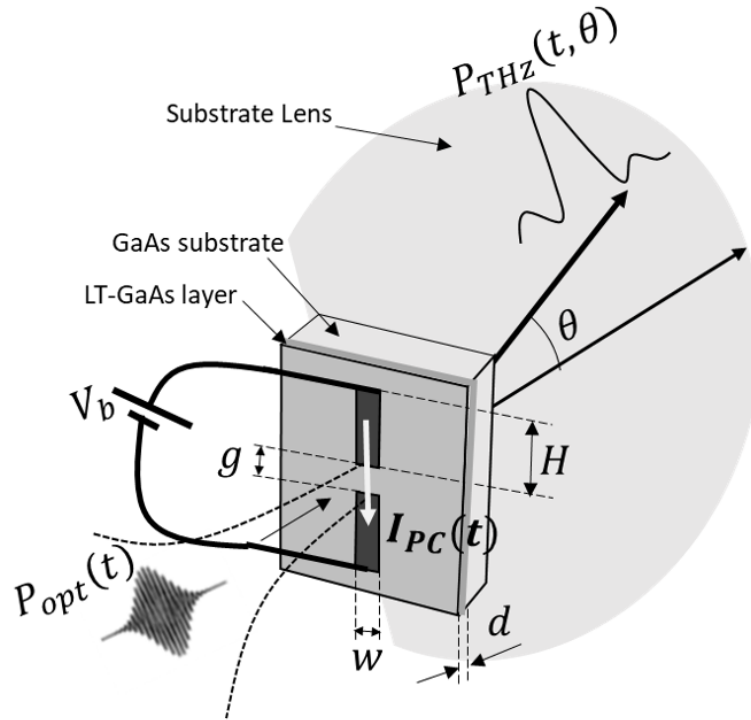
Figure 2: Scheme of a PCA generating THz radiation. The power radiated by the laser, $P_{opt}(t)$, is absorbed at the LT-GaAs layer. The generated current, $I_{PC}(t)$, radiates a THz wave due to the fast variations.

The basic principle of PCA as an emitter is to achieve a current pulse that changes in the picosecond regime to obtain a THz wave. It has four main components: the photoconductive layer, the high-resistivity substrate, the air-coupling lens, and the dipole electrodes (fig. 2). In the photoconductive layer, an incident laser pulse generates electron/hole pairs in femtoseconds. At the same time, a bias voltage applied through the electrodes accelerates the photogenerated carriers towards the electrodes. As a result, the produced photocurrent radiates feeds the antenna and radiates EM energy, according to the Maxwell equations.

The photocurrent raises at the same time as the optical pulse. After the current peaks, it decays over a time depending on the photoconductor's properties rather than the optical pulse's temporal shape. If the carriers have a long lifetime, they will contribute to the photocurrent after the pulse is absorbed. Photoconductors in PCAs, based on LT-GaAs, avoid this by having short-lived carriers [7]. In this material, the time of the pulse de-

cay occurs in the picosecond regime, which implies that the terahertz components will predominate in the radiated field.

The geometrical shape of the electrodes is a critical factor that not only affects the conversion efficiency but also the THz radiation direction pattern. Popular choices like the bow tie or H shape give a high enough directivity, but new designs such as grid-like electrodes show increased peak directivity [8].

2 PCA modelling

The basic principle for a successful model is that it should approximate the actual solution or, in experimental cases such as this one, the experimental data. However, understanding the critical processes of a system and how they interact is also particularly important when looking for a model that is not only accurate but also simple and computationally meets a trade-off between accuracy, and the ability to capture the impact of the main phenomena at play and computational efficiency. With this in mind, several researchers have proposed different models with different approximations, such as dimensionality reduction, trying to replicate the observed data. In the simplest cases, the variables such as the current density and the carrier density are assumed to be uniform in space, ignoring the effects of complex geometries. A common trait in these models is that quantities such as the carrier density, photocurrent, or charge polarization have a response function to the external stimulus.

Duvillaret et al. proposal ([12]) is based on the Drude model and neglected any non-linear response in the current as they did not consider any screening process and included the effect of collision with the lattice through a phenomenological scattering time. As a result, the data follows the obtained analytical expressions only for carrier densities smaller than $10^{18}\,\mathrm{cm}^{-3}$, and found no saturation in the photocurrent. When space charge screening is added such as in the work of Piao [22] or Jacobsen and Jepsen [18], nonlinearities in the photocurrent start to appear. They introduced space charge screening by a geometrical factor. Another type of screening called the radiation screening was also considered by Loata in his thesis [5] but he assumed that the carrier velocities reached saturation instantaneously. On the other hand, the work of Sergio Revuelta in [13] considered an instantaneous reach of the saturation velocity but including the 3D geometry and the diffusion of carriers. In this case, he observed a current saturation, but it remains to be seen the effects of radiation screening and how to include it in a simple 3D model. Also, the Drude model is often applied in a non-rigourous way, disregarding the fact that we are applying it to a variable number of particles.

2.1 Carrier density

Two phenomena determine the carrier density. On the one hand, the absorption of photons from the laser, and on the other hand, recombination. These two processes are independent and add to the total carrier variation. Here we assume that the recombination and generation are bimolecular, meaning electrons and holes recombine in pairs. Therefore, the number of electrons and holes is the same. Mobile carriers, however, include another

process that determines their free lifetime, namely trapping by imperfections. When a carrier is trapped, its velocity is zero while it still contributes towards a net charge at its location. Depending on the manufacture of the material, the material may have more or fewer impurities that decrease or increase the trapping time. In most cases, the trapping time is much shorter than the recombination time, so we use the trapping time when we talk about free carriers. Thus the density n_f of free (mobile) carriers is given by

$$\frac{dn_f}{dt} = -\frac{n}{\tau_c} + g(t) \tag{1}$$

where τ_c is the trapping time, and $g(t)$ is the generation per unit volume. τ_c may be different for electrons and holes but for simplicity, we consider it the same.

The intensity of a single Gaussian optical pulse with repetition frequency f is written as [5]:

$$I_{\text{opt}} = I_{\text{peak}} \exp\left(-4\ln(2)\left(\frac{t}{T_{\text{FWHM}}}\right)^2\right) \tag{2}$$

$$I_{\text{peak}} = \sqrt{4\log(2)/\pi}\,\frac{I_{avg}}{T_{\text{FWHM}}f}$$

$$I_{avg} = \frac{P_{avg}}{S_o}$$

Where I_{peak} is the peak intensity, I_{avg} the time-averaged intensity, T_{FWHM} is the full width at half the maximum of the intensity, P_{avg} is the time-averaged laser power and S_o the surface of the laser spot. The band gap energy E_g, absorption a, and reflectivity R determine the number of photogenerated carriers given the optical power [5].

$$g(t) = \frac{a(1-R)}{E_g} I_{\text{opt}}(t) \tag{3}$$

Equation 1 can be solved by the convolution of the generation with Green's function.

$$n_f(t) = \int_{-\infty}^{t} g(t) \exp^{-\frac{t-t'}{\tau_c}} dt' \tag{4}$$

For a Gaussian pulse excitation as in (2), (4) gives:

$$n_f(t) = \frac{a(1-R)}{E_g} \frac{P_0}{\sqrt{2}} \exp\left(t/\tau_c\right) \exp\left(\left(\frac{T_0}{2}\tau_c\right)^2\right)\left(1 - \text{erf}\left(\frac{T_0^2}{2\tau_c} - \frac{t}{T_0}\right)\right) \tag{5}$$

where we defined the new constants

$$T_0 = \frac{T_{\text{FWHM}}}{\sqrt{4 \ln 2}} \tag{6}$$

$$P_0 = P_{\text{peak}} T_0 \sqrt{\pi/2} \tag{7}$$

2.2 Drude model

In [19], it is pointed out that the Drude model for PCAs should include an extra term with respect to Duvillaret that goes unnoticed and is not explained. In this section, we derive it ourselves and understand its origin. We assume the velocity v of a single carrier follows the Drude model [21].

$$\frac{dv}{dt} = -\frac{v}{\tau_s} + \frac{qE(t)}{m} \tag{8}$$

where τ_s is the scattering time and q the charge of the carrier (e for electrons and $-e$ for holes). The current density j is the result of the movement from every free carrier:

$$j = qn_f(t)\langle v \rangle = q\frac{\sum_i^{N(t)} v_i}{\text{volume}} \tag{9}$$

is mean velocity of the carriers, v_i is the velocity of a single carrier, N(t) is the number of free carriers. As we will see, an equation similar to (8) can be derived for the mean velocity. First, we express the evolution of the mean velocity taking into account the known variation in the number of carriers:

$$\frac{d\langle v \rangle}{dt} = \frac{1}{N(t)} \frac{d}{dt} \sum_i^{N(t)} v_i - \langle v \rangle \frac{N'(t)}{N(t)} \tag{10}$$

The derivative of the sum of velocities can be expressed more rigorously by converting the sum over carriers to an integral over velocities.

$$\sum_i^{N(t)} v_i = \int_{-\infty}^{\infty} \mathcal{N}(v,t)v\,dv \tag{11}$$

$$\frac{d}{dt} \sum_i^{N(t)} v_i = \frac{d}{dt} \int_{-\infty}^{\infty} \mathcal{N}(v,t)v\,dv = \int_{-\infty}^{\infty} \frac{d}{dt}\mathcal{N}(v,t)v\,dv \tag{12}$$

$\mathcal{N}(v,t)$ is the free carrier distribution over velocities v at time t. We can substitute the total derivative with a partial derivative because the dummy variable v does not depend on time inside the integral. The time derivative of (12) can be understood as the change in the number of carriers with velocities between v and $v+\mathrm{d}v$. By analogy to hydrodynamics, we express it as the sum the particles entering the range $[v, v + \mathrm{d}v]$ and the created or destroyed particles inside $[v, v + \mathrm{d}v]$. If we approximate $\mathcal{N}(v,t)$ as being smooth, the expression for the local change in carrier distribution density $\rho(v,t) = \frac{\mathcal{N}(v,t)}{\text{volume}}$ is

$$\frac{\partial}{\partial t}\rho(v,t) = -\frac{\rho(v,t)}{\tau_c} + \mathcal{G}(v,t) - \frac{\partial}{\partial v}\left(\rho(v,t)v'\right) \tag{13}$$

The first term is the decrease of free carriers by trapping. $\mathcal{G}(v,t)$ is the carrier generation density distribution. Here we consider $\mathcal{G}(v,t) = \delta(v)g(t)$ with δ being the Dirac delta, so the generation contribution to the integral of (12) is null. The third term can be seen as the divergence of the velocity flux, v' being given by (8). The result of combining (8), (12) and (13) is

$$\frac{d}{dt}\sum_i^{N(t)} v_i = -\frac{\sum_i^{N(t)} v_i}{\tau_c} - \frac{\sum_i^{N(t)} v_i}{\tau_s} + N(t)\frac{qE}{m} \tag{14}$$

Therefore, the equation for the mean velocity, using $N' = -N/\tau_c + g(t)\cdot\text{volume}$ and (10), is

$$\frac{d\langle v\rangle}{dt} = -\frac{\langle v\rangle}{\tau_s} + \frac{qE}{m} - \langle v\rangle\frac{g(t)}{n_f(t)} \tag{15}$$

Equation 15 is the application of the Drude model to an ensemble of particles. We see an additional term with respect to the literature related to the Drude model in PCAS [12] [22] [18], to account for the newly generated carriers with zero velocity. This additional term is essential in sharp increases in the generation or low trapping times.

2.3 Electric field

There are mainly two different electric field screening processes that reduce efficiency. The first one is the space charge screening which is heavily affected by the geometry of the electrodes. The second one is radiation screening or screening due to short-range emitted fields.

The electric field inside the PCA is the result of several terms:

- the bias field E_{bias}.

- the screening of the bias field due to the space charge polarization, E_{sc}

- the screening of the bias field by the THz radiation, E_{rad}.

$$E = E_{\text{bias}} + E_{\text{sc}} + E_{\text{rad}} \tag{16}$$

In our model, we approximate the first and second terms by the result that we would obtain with parallel electrodes. While this is far from reality, we use constants that depend on the electrodes' geometry and can be fitted to experimental data. This approximation is good as long as the computed quantities don't need to be explicitly dependent on space; instead, they are effective averages.

The voltage difference between the electrodes induces the bias field. The equivalent electric field in parallel plates separated by a distance l_e is

$$E_{\text{bias}} = \frac{V}{l_e} \tag{17}$$

The charge polarization of the photoconductor represents the charge surface density separated by the electric field and accumulated around the electrodes. It is given by charge arriving at the electrodes, and the time it takes to disappear by recombination:

$$\frac{dP(t)}{dt} = -\frac{P(t)}{\tau_r} + j \tag{18}$$

where τ_r is the recombination time. Following the same principle of parallel plates approximation, we express the quasiestatic screening field as

$$E_{\text{sc}} = \frac{P(t)}{\kappa\epsilon} \tag{19}$$

where ϵ is the dielectric permittivity of the photoconductor, and κ is the screening factor. κ depends on the geometry of the electrodes and the screening efficiency.

The radiation screening can be approximated similarly by introducing the antenna impedance Z_a (figure 3). The antenna impedance Z_a describes the opposing electric field generated by the current inside the photoconductor.

$$E_{\text{rad}}(t) = -\frac{i_{\text{pc}}(t)Z_{\text{a}}}{l_e} = -\frac{j(t)S_e Z_{\text{a}}}{l_e} \tag{20}$$

with i_{pc} being in the photocurrent and S_e the surface of the electrodes.

Far from the PCA, it may be viewed as a dipole varying in time. Assuming a Hertzian dipole in an isotropic media with a refractive index $n = \sqrt{\epsilon/\epsilon_0}$, the electric field radiated from a time-dependent dipole moment $p(t)$ is [10]:

$$E(r, \phi, \theta) = \frac{1}{4\pi\epsilon} \left(\frac{1}{r^3}p(t) + \frac{n}{cr^2}\dot{p}(t) + \frac{n^2}{c^2 r}\ddot{p}(t) \right) \sin\theta \tag{21}$$

The three terms are written in the following order: the quasi-static field, the near field, and the far-field. Due to the $1/r$ dependence, the far-field will dominate at long distances from the photoconductor. Therefore the radiated is proportional to the derivative of the photocurrent and is equal to

$$E_{THz} = \frac{l_e}{4\pi\epsilon r} \frac{\partial i_{pc}(t)}{\partial t} \sin\theta \tag{22}$$
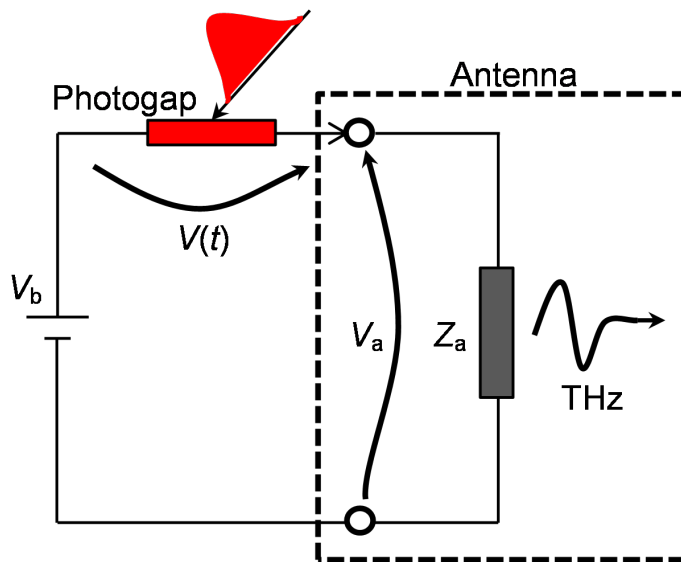
Figure 3: Schematic representing the equivalent circuit of the PCA

3 Iterative Fixed point methods

Let $\mathbf{G}$ be a vector-valued function that may be nonlinear. We define the fixed point vector $\mathbf{x}^*$ by the following equation:

$$\mathbf{G}(\mathbf{x}^*) = \mathbf{x}^* \tag{23}$$

Iterative fix point methods formally give the solution of (23) after an infinite number of steps. The idea of iterative methods is to create a sequence of vectors $\mathbf{x}^{(k)}$ that converges to the fixed point vector.

$$\mathbf{x}^* = \lim_{k \to \infty} \mathbf{x}^{(k)} \tag{24}$$

Ideally, the iteration is stopped at value of n when $||\mathbf{x}^{(n)} - \mathbf{x}^*|| < \epsilon$, where ϵ could be a fixed tolerance and $||\cdot||$ is any convenient vector norm. However, since the precise solution is clearly not available, it is necessary to introduce suitable stopping criteria to watch for the convergence of the iteration. The residual f is defined as:

$$\mathbf{f}(\mathbf{x}) = \mathbf{G}(\mathbf{x}) - \mathbf{x} \tag{25}$$

The residual of $\mathbf{x}$ is used to estimate how far $\mathbf{x}$ is from the fixed point, for example, by taking the norm.

3.1 Fixed-Point Iteration

The fixed-Point iteration is defined as

Algorithm 1 Fixed-point Iteration

Given $\mathbf{x}^0$
$k \leftarrow 0$
while $\mathbf{x}^k$ has not converged **do**
    $\mathbf{x}^{k+1} \leftarrow \mathbf{G}(\mathbf{x}^k)$
    $k \leftarrow k + 1$

The algorithm converges to the fixed-point $\mathbf{x}^*$ if $\mathbf{G}$ fulfills certain spectral conditions. The following theorems provide sufficient conditions to determine if the fixed point exists and if the fixed-point iteration will converge. For the proofs, we refer to [14].

Definition 1 *A mapping $\mathbf{G} : D \subset \mathbb{R}^n \to \mathbb{R}^n$ is a contraction on a set $D_0 \subset D$ if there exists a constant $\alpha < 1$ such that $||\mathbf{G}(y) - \mathbf{G}(x)|| \leq \alpha ||\mathbf{y} - \mathbf{x}||$, $\forall \mathbf{x}, \mathbf{y} \in D_0$*

The Contraction-mapping theorem ensures the existence of a fixed point.

Theorem 1 (Contraction-mapping theorem) *If $\mathbf{G} : D \subset \mathbb{R}^n \to \mathbb{R}^n$ is a contraction on a closed set $D_0 \subset D$ and $\mathbf{G}(\mathbf{x}) \in D_0$, $\forall \mathbf{x} \in D_0$, then $\mathbf{G}$ has a unique fixed point in D_0.*

Theorem 2 *Suppose that $\mathbf{G} : D \subset \mathbb{R}^n \to \mathbb{R}^n$ has a fixed point $\mathbf{x}^0$ in the interior of D and that $\mathbf{G}$ is continuously differentiable in a neighborhood of $\mathbf{x}^0$. Denote by $\mathrm{J}_{\mathbf{G}}$ the Jacobian matrix of $\mathbf{G}$ and assume that $\rho(\mathrm{J}_{\mathbf{G}}(\mathbf{x}^*)) < 1$. Then there exists a neighborhood S of $\mathbf{x}^*$*

such that $S \subset D$ and, for any $x^0 \in S$, the iterates x^k defined in Algorithm 1 all lie in D and converge to $\mathbf{x}^*$.

As we can see, the conditions required to ensure convergence are not guaranteed. The main problem of fixed-point iterations is that they may not converge; if they do, they may do so linearly, which is unacceptably slow for real-world applications. In that case, it is necessary to find another method. One option is to reformulate the problem as a root-finding problem to use well-known algorithms that provide better convergence. The option we choose is to use a refinement of the fixed-point iterations, the acceleration methods.

3.2 Anderson acceleration

Acceleration methods can alleviate slow convergence or even divergence. A particular acceleration method that originated in the work of Anderson is called Anderson acceleration [16]. Unlike other methods for solving nonlinear equations, such as the Newton method, Anderson acceleration does not require evaluating the Jacobian of the functional, which is usually a numerically unstable process. The algorithm for computing the fixed point $\mathbf{x}^*$ with Anderson acceleration, as stated in [15], is

---
Algorithm 2 Anderson Acceleration

Given $\mathbf{x}^0$ and $m \geq 1$
$\mathbf{x}^1 \leftarrow \mathbf{G}(\mathbf{x}^0)$
for $k = 1, 2, \ldots$ **do**
$\quad m_k \leftarrow \min\{k, m\}$
$\quad \mathbf{F}^k \leftarrow (\mathbf{f}_{k-m_k}, \ldots, \mathbf{f}_k)$ where $\mathbf{f}_i = \mathbf{G}(\mathbf{x}^i) - \mathbf{x}^i$
$\quad$Determine $\alpha^k = (\alpha_0^k, \ldots, \alpha_{m_k}^k)$ that solves $\min_\alpha ||\mathbf{F}^k \alpha||_2$ s.t. $\sum_{i=0}^{m_k} \alpha_i = 1$
$\quad \mathbf{x}^{k+1} \leftarrow \sum_{i=0}^{m_k} \alpha_i^k \mathbf{G}(\mathbf{x}^{k-m_k+i})$

The acceleration methods consider previous iterations to try to minimize the next residual. In Anderson acceleration, the minimization problem finds a linear combination of the prior iterands such that its associated coefficients also minimize the linear combination of the residuals. Intuitively, if $\mathbf{G}$ were a linear operator, it would be equivalent to the generalized minimal residual (GMRES) method [15].

Algorithm 2 is not exactly the same as Anderson's original formulation [16]. The least-squares problem was originally formulated in a unconstrained form:

$$\min_{(\theta_1, \ldots, \theta m_k)} ||\mathbf{f}_k + \sum_{i=1}^{m_k} \theta_i(\mathbf{f}_{k-i} - f_k)|| \tag{26}$$

These two formulations are equivalent, and neither is preferred in theory. In the code, we implemented a modified unconstrained form.

3.3   Practical implementation of Anderson method

There are two primary considerations when implementing algorithm 2. The first one is choosing an appropriate truncation m_k of the number of iterations taken into account. The second one is choosing an efficient way to solve the least-squares problem.

The choice of m_k must be neither too high nor too low. A low value limits the information for finding the best next iteration, decreasing the convergence rate. On the other hand, a high value might set a high condition number for the least-square problem and use too old iterations that degrade the convergence [15] and could demand large memory resources due to the need to store all the iterands.

To solve the least square problem efficiently, we use QR decomposition. The advantage of inverse solutions using QR decomposition is that they are more numerically stable than the direct matrix inverse, as evidenced by their reduced condition numbers.

The Matlab code used is the following:

Listing 1: Matlab code for Anderson acceleration

```matlab
function y =   AndersenAcceleration(f,x0,k_max,tol_res,m)
global niter;
x = [x0, f(x0)]; % Vector of iterates x.
g = f(x0) − x0; % Vector of residuals.
g = [g (f(x(:,2))−x(:,2))];

G_k = g(:,2) − g(:,1); % Matrix of increments in residuals.
X_k = x(:,2) − x(:,1); % Matrix of increments in x.

k=2;

error_estimation = Inf;
while k < k_max && error_estimation > tol_res
    m_k = min(k, m);

    % Solve the optimization problem by QR decomposition.
    [Q, R] = qr(G_k);
    gamma_k = R \ (Q' * g(:,k));

    % Compute new iterate and new residual.
    x = [x (x(:,k) + g(:,k) − (X_k + G_k) * gamma_k)];
    g = [g (f(x(:,k + 1)) − x(:,k + 1))];

    X_k = [X_k, x(:,k + 1) − x(:,k)];
    G_k = [G_k, g(:,k + 1) − g(:,k)];
    error_estimation = norm(g(:,end),2)/norm(x(:,end),2)

    n = size(X_k, 2);
    if n > m_k
```

```
        X_k = X_k(:, n − m_k + 1:end);
        G_k = G_k(:, n − m_k + 1:end);
    end
    k = k + 1;
end
niter = k−1;
y = x(:,end);
end
```

It should be noted that the form (26) is not optimal for implementation. In our code, we organize the computation differently to make the coefficient matrix easy to update by adding a column and deleting another. As suggested by [15] the following least-square problem has better conditioning and is equivalent to (26):

$$\min_{\theta \in \mathbb{R}^{m_k}} \|\mathbf{f}(\mathbf{x}^k) + \sum_{j=0}^{m_k-1} \theta_j (\mathbf{f}(\mathbf{x}^{k-m_k+j+1}) - \mathbf{f}(\mathbf{x}^{k-m_k+j}))\| \tag{27}$$

The loop stops when it reaches the maximum number of iterations or when the relative residual of x, $\frac{\|\mathbf{G}(\mathbf{x})-\mathbf{X}\|}{\|\mathbf{x}\|}$ (L_2 norm), is less than the specified tolerance.

UNIVERSITAT POLITÈCNICA
DE CATALUNYA
BARCELONATECH

UPC

telecos
BCN

```
1    Current density   ◄─┐
       │              │  │
       ▼              │  │
2    Polarization     │  │
       │              │  │
       ▼              ▼  │
3    Electric field       │
       │                  │
       ▼                  │
4    Mean velocity    ─────┘
```
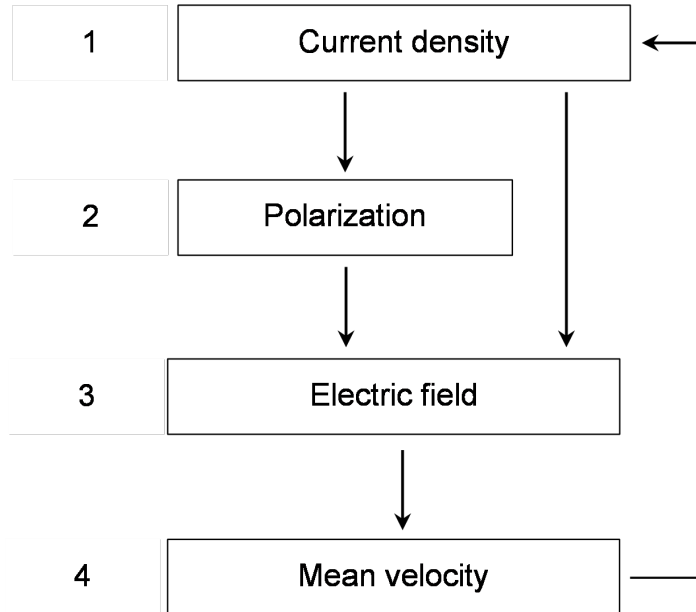
Figure 4: Cycle of dependence between the variables used for the fixed point methods

4   Application of fix point method to the model

4.1   Problem definition

The inclusion of the Drude model makes the problem very hard to solve. Indeed, the current depends on the velocity, which depends on the field, which depends on the current and the polarization (figure 4). We have a cyclic dependence that suggests the use of a fixed-point method. To define the function $\mathbf{G}$, we choose as the variable the current density time series j_t. $j_t \in \mathbb{R}^n$ is a time series whose element $j_t[i]$ indicates the values of the jt at time t_i. Thus, the dimension n of the vector corresponds to the number of time steps in which the time interval of interest is discretized. We want to transform a differential equation problem into the following fixed point problem:

$$j_t = \mathbf{G}(j_t) \tag{28}$$

Since the mean velocity is not defined at the beginning when the carrier density is zero, we use the flux of carriers variable $J(t) = \frac{\sum v_i}{\text{volume}}$ of equation (9) and (14) instead of the mean. For the discretization, we employ numerical convolution ($\circledast$), evaluating the impulse responses at the time points. Therefore, the operator $\mathbf{G}$ is defined by the following set of equations:

$$\mathbf{G}(j^t) = e\left(J_e^t - J_h^t\right) \tag{29}$$

$$J_e^t = \frac{-e}{m^e}(n_f^t E^t) \circledast (\theta(t)\mathrm{e}^{-t(1/\tau_c+1/\tau_s)})\delta t \tag{30}$$

$$J_h^t = \frac{e}{m^h}(n_f^t E^t) \circledast (\theta(t)\mathrm{e}^{-t(1/\tau_c+1/\tau_s)})\delta t \tag{31}$$

$$E^t = E_b - \frac{1}{\kappa\epsilon}P^t - \frac{Z_a}{l_e}S_e j^t \tag{32}$$

$$P^t = j^t \circledast (\theta(t)\mathrm{e}^{-t/\tau_c})\delta t \tag{33}$$

where the superscript t denotes a time series vector of the corresponding variable, and δt is the duration of every discrete time interval. Equations (29) to (33) are nothing more than the time discreet version of the model. Equations (30) and (31) are the Drude model. The operator $\mathbf{G}$ is not linear due to the presence of the bias field.

THz radiation is also computed to evaluate the emission power and spectrum.

$$E_{THz}^t = \frac{l_e}{4\pi\epsilon r}\frac{\mathrm{diff}(j^t)}{\delta t}\sin\theta \tag{34}$$

$\mathrm{diff}(j^t) = j^t[i+1] - j^t[i]$ is the difference of consecutive current values.

The spectrum is given by:

$$E_{THz}^f = \mathcal{F}(E_{THz}^t) \tag{35}$$

Where $\mathcal{F}$ is the Fourier transform.

4.2 Parameters and initial value

When choosing the parameters, we aim at realistic values that allow us to explore dependencies and compare results. As reference, the standard values around which we study the results are in Table 1.

parameter	value	parameter	value
l_e	$50\,\mu\mathrm{m}$	a	$15\,000\,\mathrm{cm}^{-1}$
S_e	$5\,\mu\mathrm{m}^2$	R	0.3
κ	900	E_g	$1.4\,\mathrm{eV}$
m^e	$0.067m_e$	V_b	$20\,\mathrm{V}$
m^h	$0.37m_e$	Z_a	$100\,\Omega$
τ_c	0.5 ps	T_{FWHM}	$0.15\,\mathrm{ps}$
τ_r	100 ps	P_{avg}	$20\,\mathrm{mW}$
τ_s	0.03 ps	S_o	$25\,\mu\mathrm{m}^2$
		f	$180\,\mathrm{MHz}$

Table 1: Values of antenna parameters .

Optical properties of GaAs are found in [17].

As shown by Theorem 2, the initial value x^0 determines whether or not the method converges. Therefore, we must try to start with a value as close as possible to the fixed point. We can use the analytical expression adapted from [18] as a first approximation:

$$j_0(t) = en_f(t) \left(E_b - E_b n_f(t) \circledast \left(\frac{e\mu}{\kappa\epsilon} \frac{\tau_c\tau_r}{\tau_r - \tau_c} (\mathrm{e}^{-t/\tau_r} - \mathrm{e}^{-t/\tau_c}) \right) \right) \tag{36}$$

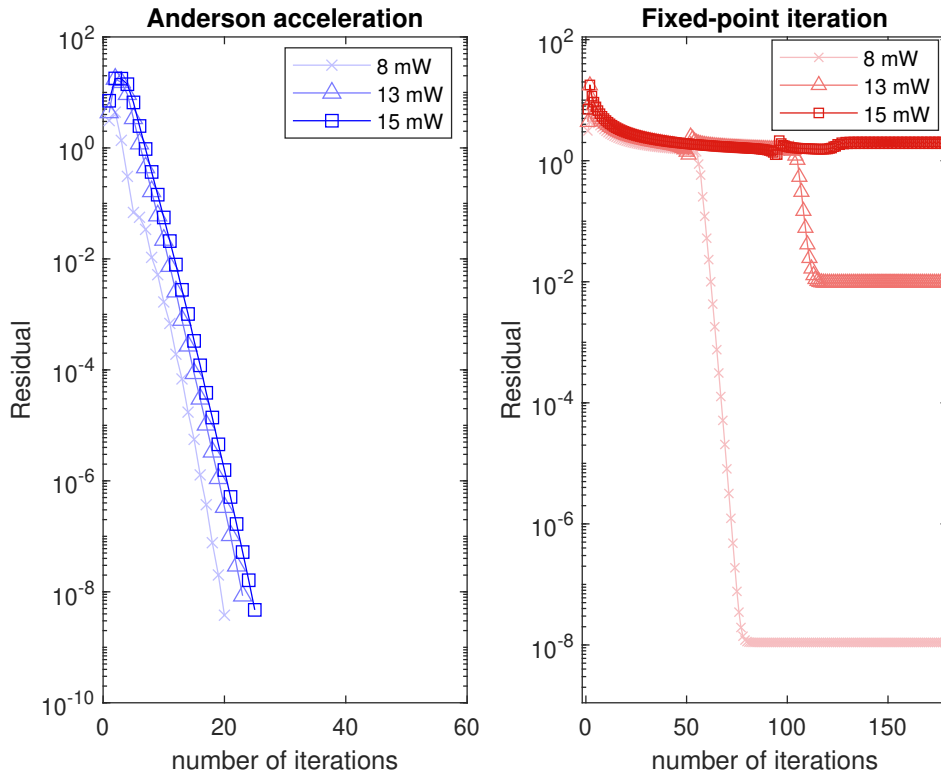This expression approximates the solution without the Drude model and only with space charge screening.

Figure 5: Evolution of the relative residual $\frac{\|\mathbf{G(x)-X}\|}{\|\mathbf{x}\|}$ for Anderson acceleration and fixed-point iteration at different optical powers, using Table 1 parameters and m = 30 and a residual tolerance of 10^{-3}.

5 Results

5.1 Convergence

We will first analyze the convergence of the two proposed methods. Starting the computations, we quickly realized that the fixed-point iteration has a relatively limited region of convergence. The results of Figure 5 show that for optical powers higher than 13 mW, the fixed-point iteration fails to converge. As expected, Anderson acceleration shows a steady exponential decrease in the residual with each iteration. Fixed-Point iteration is particularly surprising as the residual starts decreasing slowly and suddenly decreases and stagnates if the optical power is less than 13 mW. If the optical power is higher than 13 mW, the residual stays around 1, meaning that the iterand is changing significantly and it won't reach the fixed point. A good enough convergence is achieved only when the residual is much smaller than 1. The lower the optical power, the lower the level of stagnation, and the sooner convergence is achieved. With Anderson acceleration, the convergence is also faster at low optical power.

The Anderson acceleration method converges in fewer iterations than the basic fixed-point method but is slower (Figure 6). Fortunately, increasing the value of m works well to speed

UNIVERSITAT POLITÈCNICA
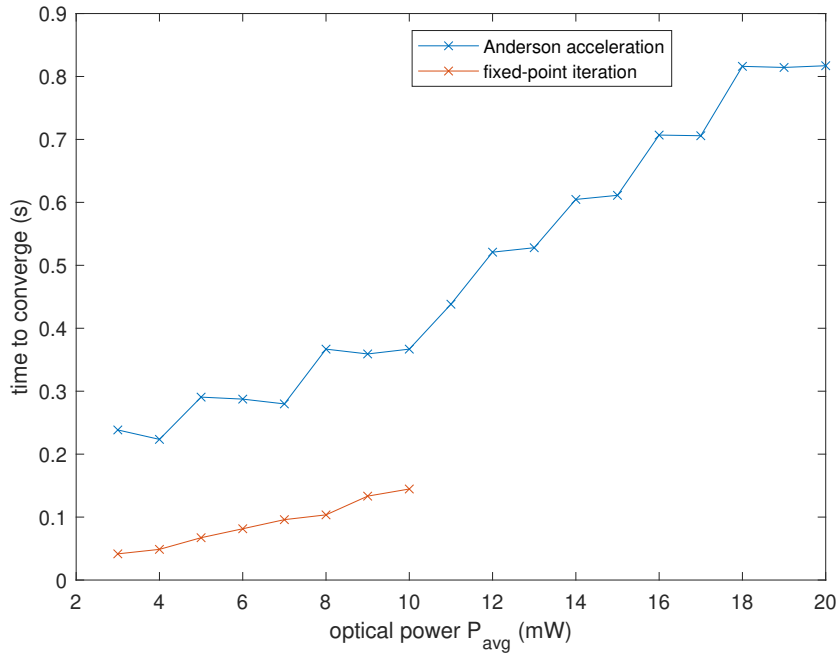DE CATALUNYA
BARCELONATECH
UPC

telecos
BCN

Figure 6: Time to converge of both methods as a function of the optical power. We used the parameters from Table 1 with $m = 30$ and a residual tolerance of 10^{-3}.

up the process at higher optical powers because fewer iterations are needed (Figure 7). m also determines if Anderson acceleration converges. When m is too low, we see the number of iterations necessary to achieve a certain error exponentially increase with the optical power (Figure 7). The broader range of convergence and the ability to fine-tune performance through m makes Anderson acceleration our preferred method.

5.2 PCA Performance

In Figure 8, we can observe the Gaussian optical pulse and the computed results. At first, the current increases as the optical pulse generates carriers. Then it decreases as the number of free carriers decays and the electric field decreases. We can observe that the initial guess correctly predicts the peak position but decreases too fast compared to the final result. This is not surprising as the expression (36) used as initial guess does not include neither radiation screening nor the delayed response of the carrier flux to the electric field.

The average current is the measured current when the optical pulse repeats at a frequency f:

$$\langle i_{pc} \rangle = f \int_0^T i_{pc} dt \tag{37}$$

Thanks to the increased convergence range offered by the Anderson acceleration, we can
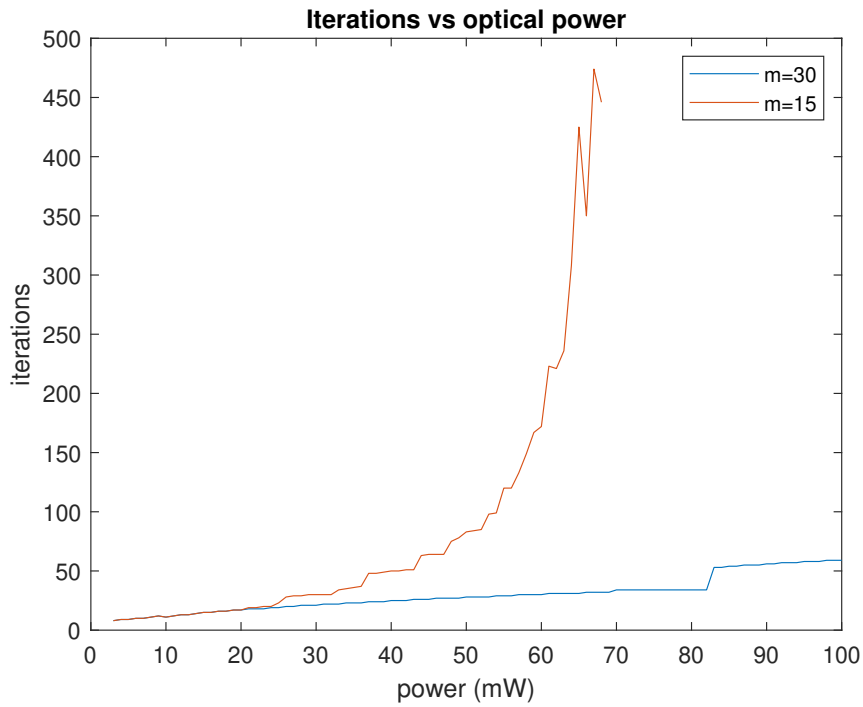
Figure 7: Number of iterations required to converge with Anderson acceleration depending on the optical power. The inputs of Algorithm 2 are $\mathbf{x}^0$ given by (36),$m = 30$ (orange line) or $m = 15$ (blue line), and a residual tolerance of 10^{-3}. The rest of parameters are the same as Table 1
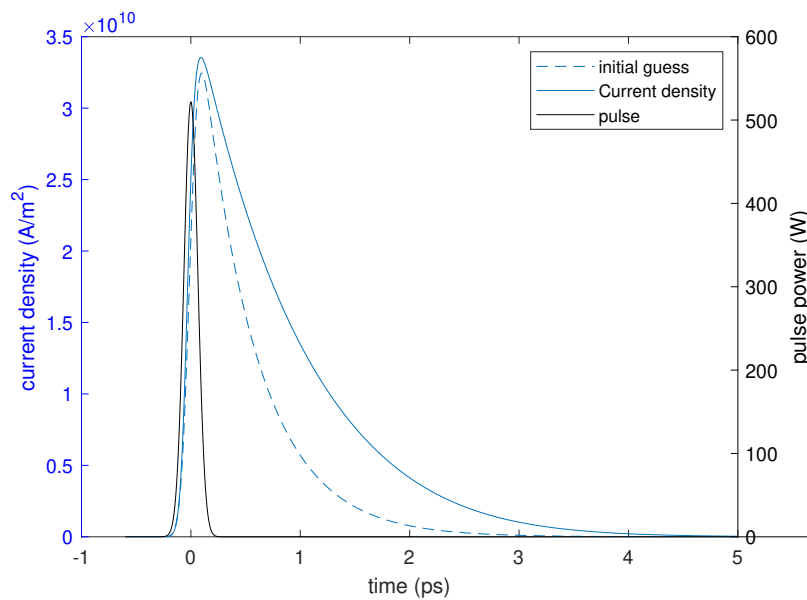

Figure 8: Pulse and computed current density with the initial guess. We used the parameters from Table 1
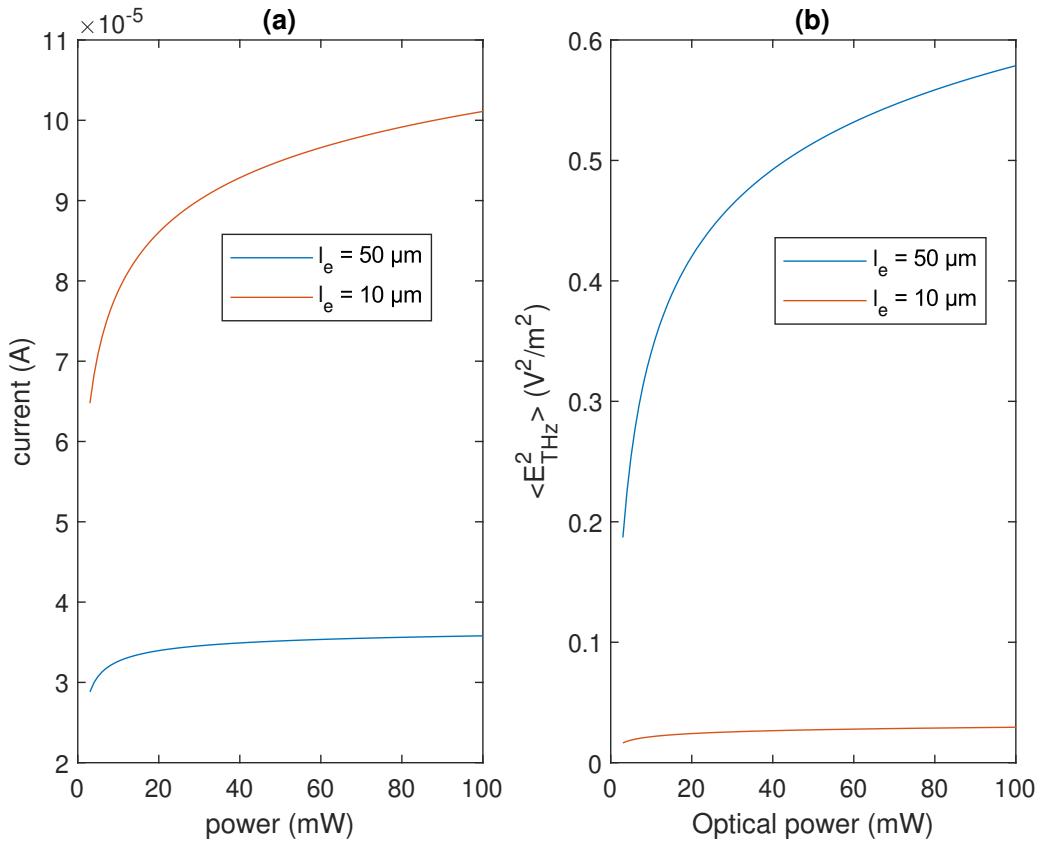
Figure 9: (a) Time averaged photocurrent $< i_{pc} >$ vs. optical power with two different gap lengths between electrodes. (b) Time average of the radiated squared electric field vs. optical power with two different gaps lengths between electrodes.

see the saturation effect of the average current (Figure 9) as the optical power increases. The same phenomenon is seen in the radiated power. Due to the saturation, the PCA is most efficient at lower optical powers.

Decreasing the gap length seems to have a positive effect, increasing the generated current (Figure 9), but actually, the radiated THz field decreases due to the shorter dipole length and the reduced current time variations.

For the frequency, we observe that the optical power significantly broadens the peak in Figure 10. On the other hand, the gap length does not affect the width; it only reduces the peak height in the spectrum (Figure 10).

5.3   Screening effects

The electric field inside the photoconductor reveals the role played by the screening. For example, in Figure 11, we see that the space charge screening is responsible for the long-living screening fields. Radiation screening, on the other hand, provides a short-lived decrease in the electric field. It should be noted that the bias field in Figure 11 is
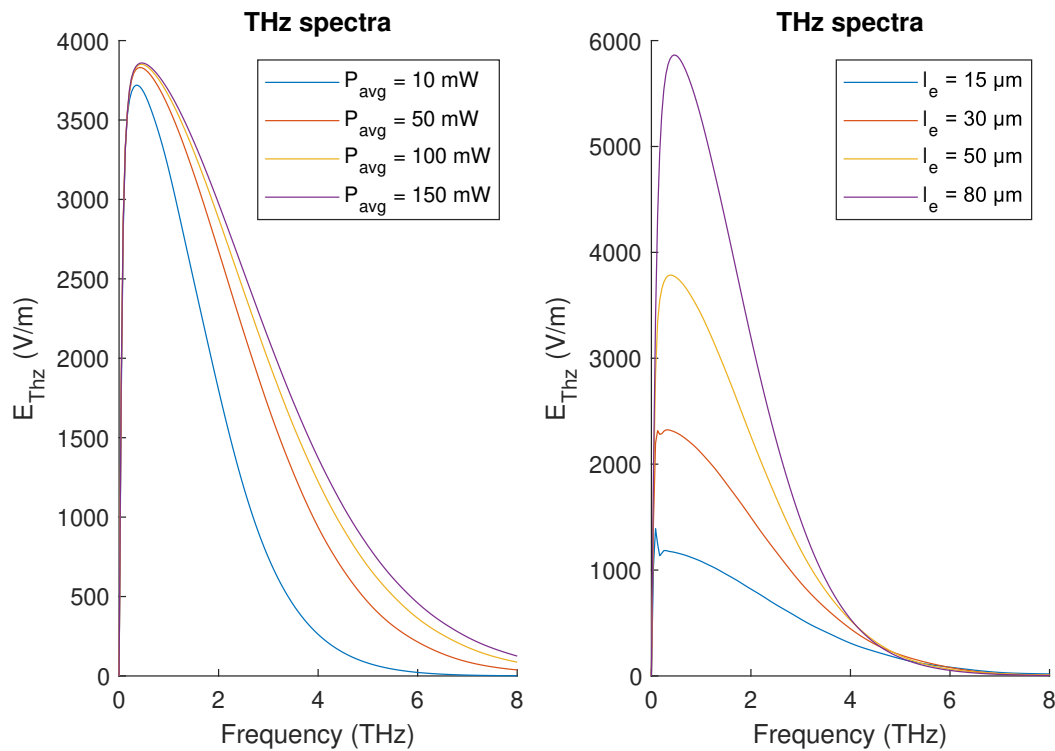
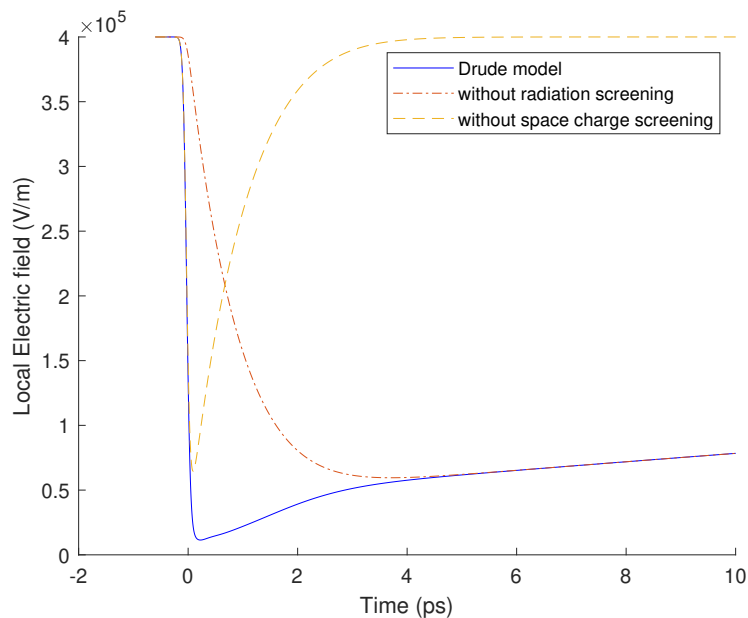Figure 10: THz spectra at different optical powers and different gap lengths.

Figure 11: Local Electric field inside the photoconductor as a function of time. The components of the field are represented by plotting without each of both screenings.
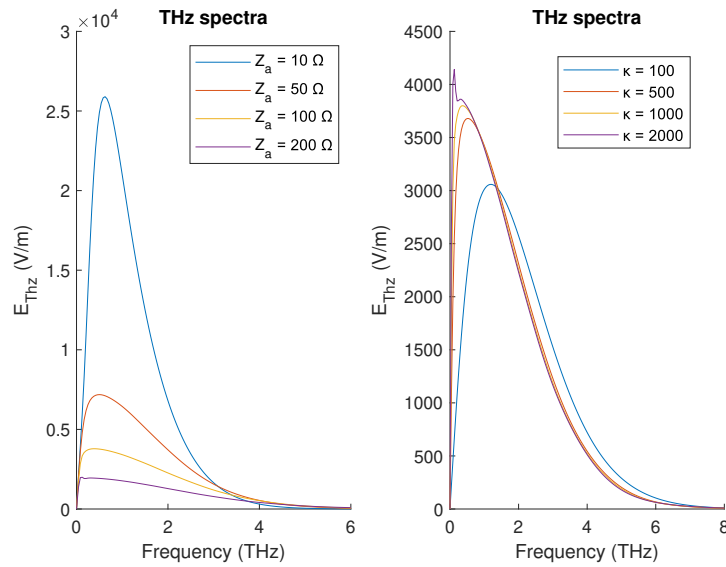
Figure 12: THz radiation spectra for different antenna impedances Z_a and geometrical factors κ.

$4\times10^5\,\mathrm{V\,m^{-1}}$. Therefore each component E_{sc} and E_{rad} can be deduced by subtracting from the bias field. These and other results regarding screening effects obtained with the Drude model using iterative fixed point algorithms will be presented in the 47th International Conference on Infrared Millimeter Wave and Terahertz Waves (IR-MMWTHz-2022) to be held in Delft from 28 August to 2 September [23].

We found that the geometrical factor affects the operational frequency of the antenna. In Figure 12, there is a clear shift of the position of the peak towards higher frequencies when decreasing the geometrical factor. Therefore a high efficiency in space charge screening will result in a higher radiation frequency but lower peak. On the other hand, the antenna impedance positively affects the THz radiation. In Figure 12, the division of Z_a by two results in almost twice the emitted THz field.

As expected, the local field shows reduced long-lived screening when κ is higher because it reduces the space charge screening (Figure 13). This effect is the opposite in the radiation screening, which increases. Additionally, we see that at low values of κ, the field switches sign. Owing to the specifics of the Drude model, the direction of the current does not change if field switches sign for a very short time (less than $0.2\,\mathrm{ps}$ in this case), as we see in Figure 13 because the radiation screening remains negative. In Figure 14, the antenna impedance Z_a presents the opposite effect; it increases the radiation screening but reduces the space charge screening. Nevertheless, in this case, the current can change direction at low impedance.

UNIVERSITAT POLITÈCNICA
DE CATALUNYA
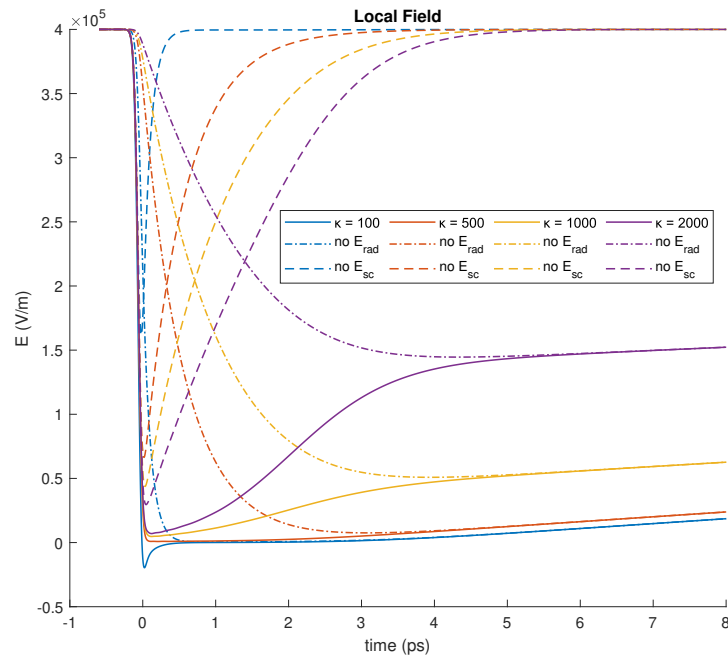BARCELONATECH
UPC

telecos
BCN

Figure 13: Local electric field inside the photoconductor as a function of time for different geometrical factors κ.
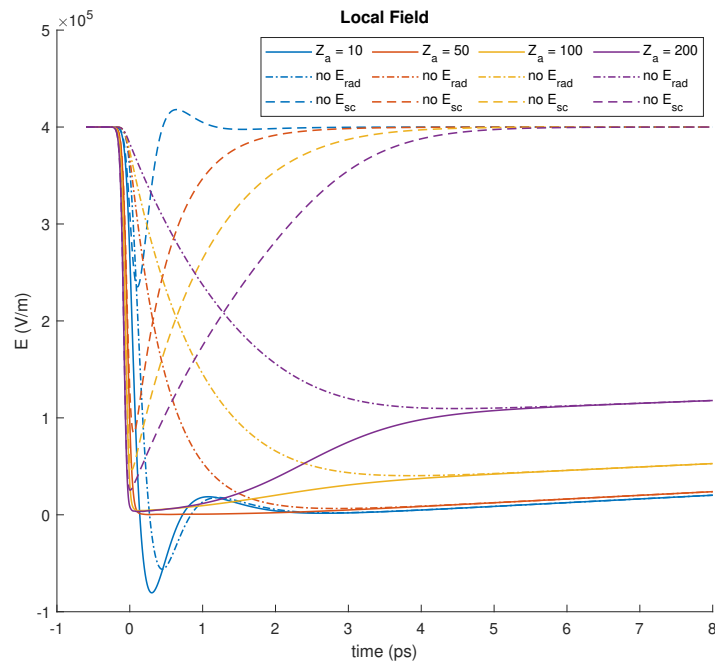

Figure 14: Local Electric field inside the photoconductor as a function of time for different antenna impedances Z_a.

6 Conclusions and future development:

In this work we have reviewed the foundations of the classical Drude model as applied to describe the dynamics of photocurrent generation and transport in Photoconductive Antennas. Bias field screening both with a space charge and radiation origin has been included. In our derivation, we take into account the effect of the generation of new carriers on the average velocity of the whole ensemble. This leads to an extra term on the classical Drude equations for PCA modeling as compared to the available literature.

The equations have been solved numerically through iterative methods. The originality of the application of iterative fixed-point methods to solution of the Drude model including screening is confirmed by acceptance of a paper at the upcoming 47th International Conference on Infrared Millimeter Wave and Terahertz Waves (IR-MMWTHz-2022) to be held in Delft from 28 August to 2 September [23] (Appendix A). The simple fixed-point method showed limited convergence, and therefore an Anderson acceleration algorithm has been implemented. Anderson acceleration provides a robust method to find the solution (current density) of the nonlinear problem. For low values of m (the number of previous iterations used) and a given error tolerance, the required iterations increased exponentially with the optical power. However adjusting the variable m to higher values around 30 was enough to ensure convergence with a relatively small number of iterations in all the relevant range of parameter values. This evidenced that Anderson acceleration is a superior method compared to fixed-point iterations.

The simulations based on the Anderson acceleration algorithm have allowed to reproduce the typical experimental results and the saturation phenomena due to bias field screening. Inside the photoconductor, the screening fields slow down the carrier dynamics. Space charge screening is responsible for long-lived screening fields whereas radiation screening produces short-lived fields. Within our model, the radiation impedance seems to decrease the radiated power and the geometrical factor is able to slightly shift the spectrum. Moreover, by analyzing the local fields we saw that the geometrical factor and the antenna impedance had opposite effects in both types of screening.

As an extension to our published work [23], a future paper contribution is already under way to include the rigorous derivation of the model and the iterative Anderson algorithm implementation. Other effects that will be interesting to study is a more precise addition of the radiation field screening that could take into account the specifics of the actual antenna imprinted over the PCA substrate. Also, the Drude models applied are based on space-averaged quantities and phenomenological factors. Further studies should consider the space dimension. Preliminar work has been conducted through a finite element simulation to compute the electric field.

By enabling a better understanding of the underlying dynamics, our results should help pave the way towards optimized design of PCAs.

References

[1] Yun-Shik Lee. *Principles of terahertz science and technology*, volume 170. Springer Science & Business Media, 2009.

[2] Giacomo Scalari, Christoph Walther, Milan Fischer, Romain Terazzi, Harvey Beere, David Ritchie, and Jerome Faist. Thz and sub-thz quantum cascade lasers. *Laser & Photonics Reviews*, 3(1-2):45–66, 2009.

[3] Peter R Smith, David H Auston, and Martin C Nuss. Subpicosecond photoconducting dipole antennas. *IEEE Journal of Quantum Electronics*, 24(2):255–260, 1988.

[4] Ho-Jin Song and Tadao Nagatsuma. Present and future of terahertz communications. *IEEE transactions on terahertz science and technology*, 1(1):256–263, 2011.

[5] Gabriel C Loata. *Investigation of low-temperature-grown GaAs photoconductive antennae for continuous-wave and pulsed terahertz generation*. PhD thesis, Citeseer, 2007.

[6] Gian Piero Gallerano, S Biedron, et al. Overview of terahertz radiation sources. In *Proceedings of the 2004 FEL Conference*, volume 1, pages 216–221, 2004.

[7] Nathan M Burford and Magda O El-Shenawee. Review of terahertz photoconductive antenna technology. *Optical Engineering*, 56(1):010901, 2017.

[8] Ning Zhu and Richard W. Ziolkowski. Photoconductive thz antenna designs with high radiation efficiency, high directivity, and high aperture efficiency. *IEEE Transactions on Terahertz Science and Technology*, 3(6):721–730, 2013.

[9] Jens Lindhard. On the properties of a gas of charged particles. *Dan. Vid. Selsk Mat.-Fys. Medd.*, 28:8, 1954.

[10] David H Auston, Kin P Cheung, and Peter R Smith. Picosecond photoconducting hertzian dipoles. *Applied physics letters*, 45(3):284–286, 1984.

[11] Ho-Jin Song and Tadao Nagatsuma. *Handbook of terahertz technologies: devices and applications*. CRC press, 2015.

[12] Lionel Duvillaret, Frédéric Garet, J-F Roux, and J-L Coutaz. Analytical modeling and optimization of terahertz time-domain spectroscopy experiments, using photoswitches as antennas. *IEEE Journal of Selected Topics in Quantum Electronics*, 7(4):615–623, 2001.

[13] Hector Lopez-Menchon, Sergio Revuelta Martínez, María C. Santos, Jordi Romeu, and Juan M. Rius. A model for photocurrent generation in photoconductive antennas. In *2019 13th European Conference on Antennas and Propagation (EuCAP)*, pages 1–4, 2019.

[14] Alfio Quarteroni, Riccardo Sacco, and Fausto Saleri. *Numerical mathematics*, volume 37. Springer Science & Business Media, 2010.

[15] Homer F Walker and Peng Ni. Anderson acceleration for fixed-point iterations. *SIAM Journal on Numerical Analysis*, 49(4):1715–1735, 2011.

[16] Donald G Anderson. Iterative procedures for nonlinear integral equations. *Journal of the ACM (JACM)*, 12(4):547–560, 1965.

[17] JO Akinlami and AO Ashamu. Optical properties of gaas. *Journal of Semiconductors*, 34(3):032002, 2013.

[18] RH Jacobsen, Karen Birkelund, T Holst, P Uhd Jepsen, and SR Keiding. Interpretation of photocurrent correlation measurements used for ultrafast photoconductive switch characterization. *Journal of applied physics*, 79(5):2649–2657, 1996.

[19] H Němec, A Pashkin, P Kužel, M Khazan, S Schnüll, and I Wilke. Carrier dynamics in low-temperature grown gaas studied by terahertz emission spectroscopy. *Journal of Applied Physics*, 90(3):1303–1306, 2001.

[20] Peter H Siegel. Terahertz technology. *IEEE Transactions on microwave theory and techniques*, 50(3):910–928, 2002.

[21] Paul Drude. Zur elektronentheorie der metalle. *Annalen der physik*, 306(3):566–613, 1900.

[22] Zhisheng Piao, Masahiko Tani, and Kiyomi Sakai. Carrier dynamics and terahertz radiation in photoconductive antennas. *Japanese Journal of Applied Physics*, 39(1R):96, 2000.

[23] David J. Schönenberger Solà, Hector Lopez-Menchon, María C. Santos, and Juan M. Rius. Impact of bias field screening and dipole length in terahertz photoconductive antennas. In *2022 47th International Conference on Infrared, Millimeter and Terahertz Waves (IRMMW-THz)*, 2022.

A

Impact of Bias Field Screening and Dipole Length in Terahertz Photoconductive Antennas

David Schönenberger, Héctor López-Menchón, María C. Santos and Juan Manuel Rius
Universitat Politècnica de Catalunya, BarcelonaTECH

Abstract- **A numerical approach for the modelling of dipole Photoconductive Antennas (PCAs) is presented, based on the classical Drude model with extension to include the bias field screening due to both the space charge and the THz radiation fields. By employing a fixed-point iterative algorithm, good computational efficiency and convergence are obtained for typical PCA configuration parameters. Results unveiling the role played by each of the different phenomena and the radiated THz spectra for different dipole lengths are shown and discussed.**

I. INTRODUCTION

BY leveraging mature optical laser technology to provide room-temperature compact devices for the advantageous generation and detection of Terahertz (THz) waves, Photoconductive Antennas (PCAs) have spurred numerous applications mainly in the fields of spectroscopy, imaging, and communications [1-2]. Notwithstanding, the extremely low optical-to-THz efficiencies reported suggest there is still huge room for improvement [2].

The classical Drude model has been extensively applied to describe the dynamics of the charge transport in PCAs including the space charge bias field screening through a phenomenological geometrical factor, whose adjustment to fit experimental observations typically yields unphysical values, around two orders of magnitude greater than expected for an ideal case. The discrepancy has been attributed to the specifics of the space charge motion transients [3]. Revision of the basic assumptions of the model and computationally efficient implementations that may shed light on the physical processes at play are found of interest.

In this paper, we describe the basis of the classical Drude approach for the modelling of PCAs including screening effects, both with a space charge field origin, following [3], and coming from the THz radiation effect, as in [4]. The coupled problem is solved with a fixed-point iterative algorithm. Fixed-point methods iteratively refine the approximation of an equation of the form $x = f(x)$ by considering an initial guess x_0 and applying the recurrence relation $x_{k+1} = f(x_k)$. Convergence is ensured if the operator $f(\cdot)$ is a contraction on a certain norm on its function space. In the case of linear operators, fixed-point methods are mathematically equivalent to the Neumann series. Due to their formal simplicity, these methods are computationally very efficient provided that the convergence conditions are fulfilled [5]. The computed photocurrent is employed in the classical dipole radiation expressions for the radiated field into a semi-infinite substrate [6]. Results for a representative PCA configuration are presented in typical PCA configuration to assess the impact of each of the phenomena involved.

II. PHOTOCURRENT MODEL

The basic structure of a PCA is shown in Figure 1. An ultrashort laser pulse is focused on the GaAs voltage-biased gap area of length g and width w in between the dipole arms of
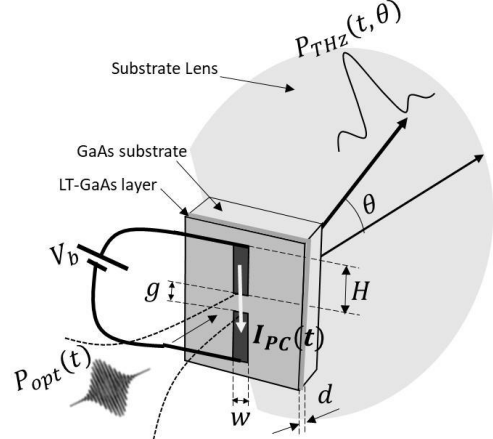

Fig. 1. Structure of the PCA.

length H. A layer of depth d grown by Molecular Beam Epitaxy (MBE) at a low temperature ensures subpicosecond lattice trapping lifetime of carriers, τ_c, for ultrafast current switching. The dipole mainly radiates towards the high-permittivity substrate ($\epsilon_r \sim 11.9$). A hyper-hemispherical high resistive silicon lens is placed to couple the THz radiation to air.

Following the classical Drude model, when the semiconductor is illuminated with photons whose energy exceeds the material's energy bandgap, E_g, electron-hole charge pairs are generated. The time dependence of the photogenerated carrier density, $n(t)$, is given by

$$\frac{dn(t)}{dt} = -\frac{n(t)}{\tau_c} + \frac{\alpha(1-R)}{wgE_g}P_{opt}(t) , \qquad (1)$$

with $P_{opt}(t)$ the time evolution of the optical pulse power and $R = \left(\frac{1-n}{1+n}\right)^2$ the air-substrate interface reflectivity, with $n = \sqrt{\epsilon_r}$ the substrate refractive index. Homogeneous illumination of the gap area $g \times w$ and exponential absorption of the pulse energy as it propagates through the GaAs substrate with optical field absorption constant α are assumed.

Under the influence of the bias field, the photogenerated carriers are accelerated towards the dipole arms. The time evolution of their average velocities, $v_e(t)$, $v_h(t)$, respectively for electrons and holes, is given by:

$$\frac{dv_{e,h}(t)}{dt} = -\frac{v_{e,h}(t)}{\tau_{se,h}} + \frac{q}{m_{e,h}}E(t) , \qquad (2)$$

with q the charge of an electron / hole, $m_{e,h}$ the effective mass of electrons / holes with typical values $m_e = 0.067\, m_0$, $m_h = 0.37\, m_0$, with m_0 the fundamental electron mass, $\tau_{se,h}$ the momentum relaxation time of electrons / holes, and $E(t)$ the electric field in the gap volume which is subject to both space charge [3-4] and THz radiation field screening [5], as follows

$$E(t) = E_b - \frac{P(t)}{\gamma\epsilon} - \frac{I_{PC}(t)}{gZ_a} , \qquad (3)$$

where $E_b = V_b/g$ with V_b the biasing voltage applied across the gap area, is the applied bias field assumed uniform in the micrometre-sized gap volume, $P(t)$ is the polarization field due to the accumulation of charge, γ is a geometrical factor which

in the ideal isotropic case takes the value $\gamma = 3$, ϵ is the permittivity of the substrate, and Z_a is the antenna radiation impedance. From (1) and (2), we may define the impulse carrier density and velocity responses, respectively as:

$$n_i(t) = \frac{\alpha(1-R)}{wgE_g} exp\left(-\frac{t}{\tau_c}\right)u(t) \qquad (4)$$

$$v_i(t) = v_{ie}(t) - v_{ih}(t) \qquad (5)$$

$$v_{ie,h}(t) = \mu_{e,h}E(t) \otimes \left(exp\left(-\frac{t}{\tau_{se,h}}\right)u(t)\right) \qquad (6)$$

where $\otimes$ denotes convolutions, $u(t)$ is the Heaviside unit step function and $\mu_{e,h} = \frac{q\tau_{se,h}}{m_{e,h}}$ represent the electron / hole mobilities. From (4)-(6) a PCA impulse photocurrent response may be defined as

$$I_{PC,i}(t) = qwd \, n_i(t)v_i(t) \qquad (7)$$

so that the instantaneous photocurrent is given by the convolution of the impulse photocurrent response and the time evolution of the optical pulse that illuminates the gap area, mathematically,

$$I_{PC}(t) = P_{opt}(t) \otimes I_{PC,i}(t) \qquad (8)$$

We assume Gaussian-like pulses, described as $P_{opt}(t) = P_{pk}exp(-4log(2)(t/T_0)^2)$, with T_0 the pulse Full Width at Half Maximum (FWHM) and power peak value P_{pk}.

The time evolution of the polarization field is given by:

$$\frac{dP(t)}{dt} = -\frac{P(t)}{\tau_r} + J_{PC}(t) \qquad (9)$$

where τ_r is the recombination lifetime of carriers, and $J_{PC}(t)$ is the photocurrent density, $J_{PC}(t) = \frac{I_{PC}(t)}{wd}$, under the usual assumption of homogeneous current distribution.

III. DIPOLE RADIATION

To find the spectrum of radiated fields in the maximum directivity direction ($\theta = 90^\circ$ in Figure 1), the Hertzian short-dipole approximation has been used [6],

$$E_{THz}(f,r) \sim \mathcal{F}\left[\frac{\mu_0 g}{4\pi r}\frac{dI_{PC}(t)}{dt}\right] \qquad (10)$$

where $\mathcal{F}[\cdot]$ denotes the Fourier transform, μ_0 is the permeability of vacuum, and f and r are respectively the frequency and distance from the PCA. To take into account the effect of the dipole length on the radiated spectrum, we use a resonant dipole approximation [6]. Because of the effect of the lens preventing back reflections and allowing efficient coupling of the wave from the substrate to air, radiation into a semi-infinite substrate may be assumed.

IV. SIMULATIONS

A fixed-point iterative numerical method is applied to solve the coupled equations given by the model. Figure 2 summarizes the outcomes for a representative PCA example with parameters displayed in the inset in Figure 2b. The impact of the different phenomena is assessed by selective switching of the terms adding their contribution to the equations. Regarding photocurrent, results in absence of screening in Figure 2a include both the assumption of instantaneous reach of the saturation velocity and gradual exponential increase with τ_s time scale, and three cases of screening: space charge only, radiation only and both space charge and radiation. The curves confirm previous observations [4], with space charge screening yielding a sudden rise and fall of the time response, smoothed

out when radiation screening is added. Also apparent is the fact that radiation screening dominates the global photocurrent behaviour. Figure 2b shows that the radiation field has a relevant impact on the polarization charge field. This is, to the best of our knowledge, the first time this extreme has been pointed out. Figure 2c shows the time evolution of the local electric field in four cases: space charge only, radiation only, both screenings and an analytical first-order approximation to include the space charge screening found in [7]. It is seen how the radiation field causes a large and sudden drop of the electric field that finally dies off giving rise to pre-eminence of space charge screening, which causes a slower time evolution of the electric field, in the longer term. Figure 2d shows the effect of the dipole length with all the effects included with the characteristic shift of the resonance peak as the dipole length changes. Extensive testing of our fixed-point algorithm reveals
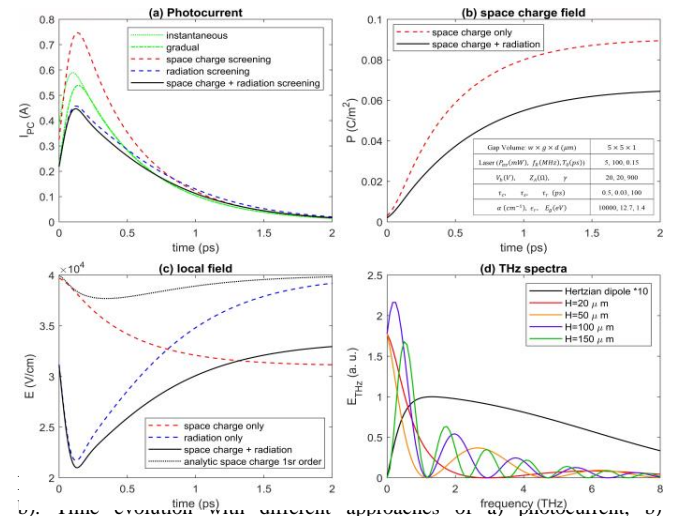

b). Time evolution with different approaches of a) photocurrent, b) polarization space charge field, c) electric field, and d) radiated spectra for different dipole lengths.

that for the typical PCA, the convergence is compromised for optical average powers beyond $5 \, mW$, whereas PCA developments may work with power levels up to $20 \, mW$.

The analysis and results presented show great promise to help research in improved PCA designs, but a further numerical investigation is required and the efficacy of refined iterative methods to extend the parameter convergence range explored.

REFERENCES

[1] H. Elayan *et al.*, "Terahertz Band: The Last Piece of RF Spectrum Puzzle for Communication Systems", *IEEE Open Journal of the Communications Society*, vol. 1, pp. 1-32, 2019..

[2] N. M. Burford and M. O. El-Shenawee, "Review of terahertz photoconductive antenna technology", *Opt. Eng.*, vol. 56, no. 1, 2017.

[3] P. Uhd Jepsen, R. H. Jacobsen, and S. R. Keiding, "Generation and detection of terahertz pulses from biased semiconductor antennas*", J. Opt. Soc. Am. B*, vol. 13, 2424-2436, 1996.

[4] G. C. Loata, M. D. Thomson, T. Loffler, and H. G. Roskos, "Radiation field screening in photoconductive antennae studied via pulsed terahertz emission spectroscopy", *Appl. Phys. Lett.*, vol. 91, no. 23, 2007.

[5] A. Quarteroni, R. Sacco, F. Saleri, "Numerical Mathematics", *Springer*, vol. 37, 2010.

[6] A. Cardama, L. Jofre, J. M. Rius, J. Romeu and S. Blanch, "Antenas", *Ediciones UPC*, 2002

[7] R. H. Jacobsen, K. Birkelund, T. Holst, P. Uhd Jepsen and S. R. Keiding, "Interpretation of photocurrent correlation measurements used for ultrafast photoconductive switch characterization", *J. Appl. Phys*, vol. 79, pp. 2649- 2657, 1996.